Published in final edited form as:
Lab Chip. 2019 September 10; 19(18): 2993–3010. doi:10.1039/c9lc00253g.

Synchronized Stimulation and Continuous Insulin Sensing in a Microfluidic Human Islet on a Chip Designed for Scalable Manufacturing

Aaron L. Glieberman[†,a], **Benjamin D. Pope**[†,a], **John F. Zimmerman**[a], **Qihan Liu**[a], **John P. Ferrier Jr.**[a], **Jennifer H. R. Kenty**[b], **Adrian M. Schrell**[c], **Nikita Mukhitov**[c], **Kevin L. Shores**[a], **Adrian Buganza Tepole**[a], **Douglas A. Melton**[b,d], **Michael G. Roper**[c], **Kevin Kit Parker**[*,a,d]

[a]Disease Biophysics Group, Wyss Institute for Biologically Inspired Engineering, Harvard John A. Paulson School of Engineering and Applied Sciences, Harvard University, Cambridge, MA 02138, USA.

[b]Harvard Department of Stem Cell and Regenerative Biology, Cambridge, MA 02138, USA.

[c]Department of Chemistry and Biochemistry, Florida State University, Tallahassee, FL 32306, USA.

[d]Harvard Stem Cell Institute, Cambridge, MA 02138, USA.

Abstract

Pancreatic β cell function is compromised in diabetes and is typically assessed by measuring insulin secretion during glucose stimulation. Traditionally, measurement of glucose-stimulated insulin secretion involves manual liquid handling, heterogeneous stimulus delivery, and enzyme-linked immunosorbent assays that require large numbers of islets and processing time. Though microfluidic devices have been developed to address some of these limitations, traditional methods for islet testing remain the most common due to the learning curve for adopting microfluidic devices and the incompatibility of most device materials with large-scale manufacturing. We designed and built a thermoplastic, microfluidic-based Islet on a Chip compatible with commercial fabrication methods, that automates islet loading, stimulation, and insulin sensing. Inspired by the perfusion of native islets by designated arterioles and capillaries, the chip delivers synchronized

---

[*] To whom correspondence should be addressed at: Pierce Hall, 29 Oxford Street, Cambridge, MA 02138, USA. Tel: +1 6174952850; Fax: +1 6174959837; kkparker@seas.harvard.edu.

[†] These authors contributed equally to this work.

Author contributions
Conceptualization: A.L.G., B.D.P., K.K.P., M.G.R., D.A.M.
Investigation: A.L.G., B.D.P., J.H.R.K.
Methodology: A.L.G., B.D.P., M.G.R., A.M.S., N.M., J.H.R.K.
Formal Analysis: A.L.G., Q.L., A.B.T., K.L.S.
Software: A.L.G., B.D.P., J.F.Z., K.L.S., A.B.T., A.M.S., J.P.F.
Visualization: A.L.G., B.D.P., J.F.Z.
Supervision: K.K.P., M.G.R., D.A.M.
Writing - Original Draft: A.L.G., B.D.P.
Writing - Review and Editing: K.K.P., M.G.R., D.A.M., Q.L., J.F.Z., A.M.S., N.M., K.L.S.

Conflict of Interest

The authors are named inventors on pending patent applications PCT US16/62693 (A.L.G., B.D.P., K.L.S., K.K.P.) and PCT US18/15601 (A.L.G., J.F.Z., J.P.F., K.K.P.) filed by Harvard University. K.K.P. is a principal at KK Parker & Associates, with consulting responsibilities to several biotech and pharma companies.

glucose pulses to islets positioned in parallel channels. By flowing suspensions of human cadaveric islets onto the chip, we confirmed automatic capture of islets. Fluorescent glucose tracking demonstrated that stimulus delivery was synchronized within a two-minute window independent of the presence or size of captured islets. Insulin secretion was continuously sensed by an automated, on-chip immunoassay and quantified by fluorescence anisotropy. By integrating scalable manufacturing materials, on-line, continuous insulin measurement, and precise spatiotemporal stimulation into an easy-to-use design, the Islet on a Chip should accelerate efforts to study and develop effective treatments for diabetes.

Keywords

Insulin Sensing; Microfluidics; Hydrodynamic Trapping; Human Pancreatic β Cells

Introduction

The physiological range of glucose in human blood is maintained in part by β cells within pancreatic islets of Langerhans, which secrete insulin in response to glucose and other stimuli [1]. Insulin secretion from cadaveric islets or, more recently, stem cell derived islet products [2] is routinely measured as a test for therapeutic potency before islet transplantation [3] and in research applications where β cells are used for diabetes modeling [4] or for studying basic islet biology [5]. The most popular method for measuring insulin secretion involves large numbers of islets that are manually aliquoted, extensive liquid-handling, and enzyme-linked immunosorbent assays (ELISAs) that require significant processing time.

The application of microfluidics to islet testing is a promising approach due to the inherent low sample and reagent volume requirements, as well as opportunities for automation and real-time readouts. Several groups have developed microfluidic assays to evaluate islet function [6,7] including cell membrane capacitance and cytoplasmic conductivity [8], fatty acid oxidation [9], oxygen consumption [10], calcium flux [11,12], and insulin secretion [13–27] The capabilities of these systems also confer powerful advantages beyond what would be practical with traditional tools. For example, many offer single-islet sensitivity [13,14,28] that minimizes the number of islets required for testing, sub-minute temporal resolution for analysis of fine timescales, and automated glucose modulation to deliver physiologically-relevant stimuli [29] Despite all the advantages of the microfluidic devices that have been developed, traditional liquid-handling followed by ELISA quantification remains the predominant method for islet testing. Adoption of microfluidic platforms has been hindered by the steep learning curve for use and the incompatibility of device materials with commercial fabrication methods. Thus, easy-to-use devices manufactured from scalable manufacturing materials could allow broader adoption of the powerful capabilities that microfluidics provide for islet testing.

Here we present a fully integrated, thermoplastic “Islet on a Chip” designed for scalable manufacturing, automated loading of islets into parallel channels, synchronized nutrient stimulation, and continuous insulin sensing based on an on-chip immunoassay quantified by fluorescence anisotropy [15]. We describe quantitative models that were used to guide device design and empirical validation of design elements, including the trapping mechanism for automated capture of islets, simultaneous propagation of dynamic stimuli across parallel islet channels, and, finally, the quantification of insulin secretion rates from human cadaveric islets.

Materials and Methods

Microfluidic Chip Design and Fabrication.

Design criteria for the microfluidic device included 1) the ability to automatically isolate and capture islets into their own designated perfusion lines, 2) parallel delivery of dynamic chemical signals to the chip, and 3) continuous quantification of insulin secreted from cells on the chip (Table 1). The first criterion was accomplished using a parallel arrangement of hydrodynamic traps dimensioned to capture individual islets, each with its own channel branching from the main perfusion channel. Two inlets allowed the delivery of dynamic signals to the chip by mixing low and high concentrations of either insulin standard (during insulin calibration) or glucose (during glucose stimulation). Inlets and mixing regions were incorporated for sequentially adding fluorescently-labelled insulin (FITC-insulin) and insulin antibody to insulin secretions on the chip, while a glass capillary was embedded on the chip for optical measurements. Together, these features provided the ability to continuously detect insulin from islets in stimulated in parallel (Figure 1).

Computer aided design (CAD) files of the chip were generated using Solidworks Premium 2017 (Dassault Systèmes, Vélizy-Villacoublay, France) for both modeling (Figure 2) and fabrication. All computational fluid dynamics was done with COMSOL versions 5.0, 5.3 a, and 5.4 (COMSOL, Inc., Burlington, MA). Corresponding modeling parameters are outlined in Table S1. Chip layers were cut on a Roland MDX-540 Modela Pro II CNC mill (Roland DGA, Irvine, CA) out of polycarbonate stock material (McMaster-Carr Supply Company, Elmhurst, IL). After sanding the faces of the chip on a flat granite block with 400 and then 600 grit sand paper, the layers were cleaned by submerging in isopropanol (VWR, Radnor, PA) and sonicating for 20 minutes. The layers were then removed and dried using an air gun. Following cleaning, the chip pieces were polished on all sides with a quick treatment of heated dichlorom ethane (Sigma-Aldrich) vapor ejected from a nozzle and left to sit in a chemical hood for at least 1 hour. A 25 mm section was cut from a 50 mm long borosilicate glass microcapillary with a square 500 µm x 500 µm inner cross section and a wall thickness of 100 µm (VitroCom, Mountain Lakes, NJ) on an Epilog Laser Mini 30W CO_2 laser cutter (Epilog Laser, Golden, CO). 1 mm long sections of 0.51 mm ID Pharmed tubing (Cole Parmer, Vernon Hills, IL) were cut with a razor and manually fit around each end of the glass capillary to serve as gaskets. After rinsing the capillary with isopropanol and drying it with an air gun, the capillary was then placed into the accommodating grooves of the bottom chip layer. Chip layers were fit together using alignment posts and sandwiched between 3/16” thick borosilicate glass panes, silicone mats and finally steel shims. The entire assembly was placed within a Carver 3895 hydraulic press (Carver Inc., Wabash, IN) and preheated to 146°C.

For bonding, a pressure of 0.42 MPa was applied for 30 minutes at this temperature. While the same pressure was maintained, the chip was then allowed to cool to room temperature for 4–5 hours.

Human Islets and SC-β Cells.

Human cadaveric islets were obtained from Prodo Laboratories (Aliso Viejo, CA) with appropriate consent and were rendered anonymous (Table S2). Purity by count was greater than 80%. Upon arrival, islets were cultured at least one day in a low adhesion plate with CMRLS 1066 (Stratech Scientific Ltd., Suffolk, England, Cat. #99–603-CV-CEG) supplemented with 1:100 GlutaMAX (Gibco, Cat. #35050061), 100 U/mL Penicillin/streptomycin, and 10% fetal bovine serum. Stem-cell derived β (SC-β) cells were differentiated as described previously [30]. For all islet and SC-β cell handling, wide bore pipette tips (VWR) were used to minimize shear. Islets and SC-β cell clusters were filtered to remove clumps but not size-selected prior to chip loading. The Committee on the Use of Human Subjects of the Institutional Review Board at Harvard University determined this work was not human subjects research.

Assay Buffer and Reagents.

All experiments were conducted in islet assay buffer (KRB; 128 mM NaCl, 5 mM KCl, 2.7 mM CaCh, 1.2 mM MgSO4, 1 mM Na_2PO_4, 1.2 mM KH_2PO_4, 5 mM $NaHCO_3$, 10 mM HEPES, 0.1% Bovine Serum Albumin, and 100 U/mL Penicillin/streptomycin) filter sterilized with a 0.22 μm filter.

Computational Design and Empirical Chip Testing

Hydrodynamic trapping: A hydrodynamic islet trap consists of a location in a flow path where flow is split between two features: a trapping region - a constriction in the channel smaller than an average islet – and a side channel or shunt that circumvents flow around the trapping region, with channel dimensions large enough for passage of islets. The design should be such that an islet flowing through the chip is delivered to the trapping region when the hydrodynamic resistance to flow in this region is initially lower compared to the shunt. In this case, the islet becomes immobilized at the constriction since it cannot pass through. Once an islet is trapped, however, the hydrodynamic resistance to flow past the islet and the trapping region should be greater than flow through the side channel to allow for subsequent islets flowing through to pass around the captured islet and exit the chip.

Multiple trap designs with different size, geometry and constriction type were compared by calculating ratios of flow rates through the trapping region and shunt (Q_{trap}/Q_{shunt}) simulated in three-dimensional Navier-Stokes flow using COMSOL. The trap with the highest proportion of estimated flow through the trapping region was fabricated into a prototype and tested using ~250 μm diameter clusters of SC-β cells as a surrogate for human islets. A combined Navier-Stokes and Brinkman flow simulation was used to estimate the added resistance of an islet captured within a single trap, modeled as a porous sphere of 200 or 250 μm in diameter (porosity of 0.1 and permeability of 1E-15 m^2) placed within a three-dimensional drawing of the trap (Figure 2b). The pressure drop across the trap was computed in each case, as well as the situation without an islet present, and the pressure drop was used to solve for the hydrodynamic resistance according to the equation:

$$R_{h,\,trap} = \frac{\Delta P_{trap}}{Q_{trap}} \tag{1}$$

where $R_{h,trap}$ is the hydrodynamic resistance of the trapping region, ΔP_{trap} is the pressure drop across the feature, and Q_{trap} is the flow rate through the feature. Resistance of the trap region, consisting of one vacant plus fifteen occupied traps, was then calculated using a two-dimensional Navier-Stokes model of flow through a planar projection of the chip lacking a side channel (Figure 2c). Because the shunt is an alternative flow path to the main channels in the chip in addition to the trapping region, the resistance of the downstream channels was also estimated. For a given length of channel with a rectangular cross section, the hydrodynamic resistance is given by the formula:

$$R_h = \frac{12\mu L\alpha}{h^4\left[1 - \sum_{n,\,odd}^{\infty} \frac{192\alpha}{(n\pi)^5} \tanh\left(\frac{n\pi}{2\alpha}\right)\right]} \tag{2}$$

where μ is the dynamic viscosity, L is the length of the channel, and α is the aspect ratio of the channel($\alpha = \frac{h}{w}$, where h is channel height and w is channel width). Calculations of a sample channel resistance for the series from 1 to 50 terms in the sum demonstrated that the first term of the series is a close approximation of the true solution, such that:

$$R_h \approx \frac{12\mu L\alpha}{h^4\left[1 - \frac{192\alpha}{(\pi)^5} \tanh\left(\frac{\pi}{2\alpha}\right)\right]} \tag{3}$$

Assuming $h = 0.4$ mm, $w = 0.4$ mm for all channels but the capillary (which had $h = 0.5$ mm and $w = 0.5$ mm) and μ, = 6.913E-4 Pa*s for water at 37 °C, the resistance of each length of channel outside of the trap region (i.e. mixing channels, capillary, and outlet) was computed. The total shunt resistance was taken to be equal to the total resistance of a chip containing fifteen islets and shunt length calculated from Eqn. 3 for a channel with $h = 0.4$ mm and $w = 0.4$ mm (Figure 2d). Trapping success was predicted using a stochastic simulation in

MATLAB that considered the probability for each successive islet being captured by a trap to be a result of the relative flow through that trap compared to the total flow. Each islet "capture" updated the resistance for that trap for successive iterations, with the islet volume within each trap assumed to be inversely proportional to the flow. Islet resistances were estimated from the three-dimensional COMSOL flow simulations of a single trap containing simulated islets of different size. For the trapping algorithm, islets of either 150 μm or 400 μm diameter were simulated, and the number of islets within each trap after full occupancy was computed for 10,000 simulation runs. These results were plotted as histograms in Figure S1 against a zero-truncated Poisson distribution computed for each simulation based on its respective mean. The mean, distribution, and mean-matched, zero- truncated Poisson distribution were also obtained from empirical trapping results after two loading experiments (n = 39 capture events in 26 traps). A sample size of 160,000 (16 traps per simulation for 10,000 simulations) was used for loading simulations. Each distribution was compared against its mean-matched Poisson distribution using a Chi-square Goodness of Fit test and Two-sample Kolmogorov-Smirnov tests were used to compare empirical and simulated distributions.

Shear stress: Shear stress was calculated for a 200 or 250 μm diameter islet (porosity of 0.1 and permeability of 1E-15 m^2) under combined Navier-Stokes and Brinkman flow (Figure 2b) according to:

$$\tau = \mu \nabla \overrightarrow{u} \tag{4}$$

where **τ** is the shear stress, μ is the dynamic viscosity, and $\overrightarrow{u}$ is the flow velocity vector.

Parallel flow: In order to achieve parallel delivery of media and stimuli to islets trapped on the chip, it was necessary to ensure that flow was split evenly to all perifusion channels. Stimulus synchronization was simulated using a two-dimensional, time-dependent model of convection and diffusion in Navier-Stokes flow within a planar projection of the chip (Figure 2f). Empirical validation of parallel delivery was conducted using a solution of 1.72 mM 2-(*N*-(7-Nitrobenz-2-oxa-1,3-diazol-4-yl)-Amino)-2-Deoxyglucose (2-NBDG; Sigma-Aldrich, St. Louis, MO), a fluorescent glucose analog. A PCO Panda 4.2 sCMOS camera (PCO AG, Kelheim, Germany) was used to record videos of fluorescent pulses of 2-NBDG and time to reach each trap, duration of each pulse, maximum pulse intensity, and a kymograph were calculated within each channel using ImageJ.

Glucose and reagent mixing: Glucose mixing on the chip was first assessed by scaling law approximations. The time for complete mixing of a species to occur due to diffusion, t_{mixing}, can be approximated as:

$$t_{mixing} \sim \frac{w^2}{D}$$

(5)

where w is the width of the channel and D is the diffusivity of the species. Time for a species flowing through a rectangular channel to traverse a given length, L, of the channel is given as:

$$t_{travel} = \frac{whL}{Q}$$

(6)

where h is the height of the channel and Q is the volumetric flow rate. Setting these two equations equal, the length of channel needed to fully mix a species across the width of that channel is given as:

$$L_{mixing} \sim \frac{wQ}{hD}$$

(7)

Mixing length for glucose was estimated for a channel with a 0.4 mm x 0.4 mm cross section (width x height) using 4E-10 m^2/s [31] as the diffusivity of glucose and 1 μL/min as the flow rate. A three-dimensional model of convection and diffusion under Navier-Stokes flow was also used to simulate glucose mixing with 20 mM glucose applied to one inlet and 0 mM glucose applied to the other (Figure 2a). Based upon the results of the model, a mixing motif was incorporated into the final chip with a length of channel necessary for mixing. To validate glucose mixing, the same approach described for testing parallel flow was utilized. Since mixing length is inversely proportional to species diffusivity (Eqn. 7), channel lengths required to mix insulin and insulin antibody were similarly estimated using diffusivities of 11.6E-11 m^2/s [32] and 2.8E-11 m^2/s, respectively (Figure 2e). The latter number was estimated from the Stokes-Einstein equation, which describes a relationship between diffusivity and effective radius of a particle:

$$D = \frac{k_B T}{6\pi\mu r}$$

(8)

where, k_B is the Boltzmann constant, T is temperature, μ is the dynamic viscosity of the solution, and r is the effective particle radius.

The diffusivity of insulin antibody was estimated from Eqn. 8 using the diffusivity of insulin and the relative radii of the two species [33]. The diffusivity of FITC-insulin (10.9E-11 m^2/s) was similarly estimated from the molecular radius of fluorescein[34]. Mixing channels with lengths calculated in this manner were incorporated into the final chip design. Empirical validation of mixing for FITC-insulin and insulin antibody was conducted by flowing 1.6 μM solutions of FITC-insulin (Sigma-Aldrich, Cat. #I3661) and Alexa Fluor 647 secondary antibody (Thermo Fisher, Cat. #A-21235) into their respective reagent inlets at flow rates of 0.1 μL/min. Tiles scans were made in brightfield and of each fluorescent channel to capture the steady state location of FITC-insulin and antibody within the mixing regions. Images were analyzed in ImageJ for fluorescent intensity across the width of the channel at different points along the channel length.

Oxygenation and viability: Oxygenation of islets was determined by comparing an estimate of per-islet oxygen consumption [3.6 pmol/min*islet [35]] with a calculated delivery of oxygen in the microfluidic device (24.3 pmol/min*trap), which takes into account the estimated concentration of atmospheric oxygen in culture medium at 37 °C from Henry's law [177.66 μM [36]] and the flow rate in the device per trap (0.0875 μL/min). Hypoxia was also assessed empirically with BioTracker 520 Green Hypoxia Dye (EMD Millipore, Cat. #SCT033). A working solution of 5 μM was prepared in either CMRLS or KRB containing 2.8 mM glucose and islets were suspended in dye solution either on the same day as being received or after a night of incubation in CMRLS to allow for recovery. Following dye treatment, all islets were rinsed once with PBS, re-suspended in medium, and imaged after at least 1 hour of additional incubation time. A portion of islets that had been treated in the KRB were loaded onto a chip with 2.8 mM glucose in KRB flowing at 1.4 μL/min and were exposed to this buffer for roughly 70 minutes on a setup similar to that used for glucose stimulation (see Islet Loading and Glucose Stimulation). Then a pulse of 20 mM glucose in KRB was delivered for 70 minutes. Fluorescent images of islets on the chip were taken during incubation in 2.8 mM glucose, at the initial onset of the 20 mM glucose pulse, and at 30 minutes and 70 minutes following introduction of 20 mM glucose. Afterwards, suction was applied to the glucose inlet to retrieve islets that had been captured on the chip. These islets, along with islets that had remained in CMRLS since arrival of the isolation and that had not been treated with dye, were live-stained with 2 μg/mL Hoechst (Life Technologies, Cat. #H3570) and 1 μg/mL propidium iodide (Sigma-Aldrich, Cat. #P4179–100MG) for 30 minutes. A portion of the islets that had remained in culture were stained in PBS + 0.1%

Triton X-100 to permeabilize the membrane and serve as a positive control for propidium iodide staining. All islets were imaged for Hoechst and propidium iodide fluorescence.

Insulin secretion and signal propagation: Insulin secretion rates were estimated from average insulin secretion by human islets and SC-β cells before and after glucose stimulation. Briefly, islets were incubated in transwells for 1 hour at 37°C in KRB lacking pen/strep with 2.8 mM glucose, followed by two sets of alternating 1 hour treatments of 2.8 mM glucose and 20 mM glucose. Secreted insulin was quantified by an Alpco Ultrasensitive Human Insulin ELISA (ALPCO, Salem, NH). To quantify secretion rates, one IEQ was assumed to contain 1560 cells [37] Human islets produced insulin at 1.3E-1 μIU/IEQ*min in 2.8 mM glucose and 3.9E-1 μIU/IEQ*min in 20 mM glucose, while SC-β cells produced 2.6E-2 μIU/IEQ*min and 1.3E-1 μIU/IEQ*min, respectively. Using 2-minute measurements from a perifusion system (Biorep) delivering 0.1 mL/min of KRB with either 2.8 mM or 20 mM glucose, human islets secreted 1.1E-1 μIU/IEQ*min and 1.1 μIU/IEQ*min, while SC-β cells secreted 6.8E-3 μIU/IEQ*min and 5.6E-1 μIU/IEQ*min, respectively. Using IEQ, the insulin secretion rates above, and a flow rate per islet of 0.0875 μL/min, expected insulin concentrations on the chip were estimated. The flow rate was selected assuming one islet per trap to ensure that, with minimal trap filling, insulin levels would be detectable. Propagation of the insulin signal from trapped islets or during calibration was modeled as done for glucose pulse synchronization (see Parallel flow), using insulin diffusivity (see Glucose and reagent mixing) and tracking time-dependent insulin concentration at the capillary (Figure 2g). Accounting for diffusion during signal propagation, an overall range of 1–30 mlU/mL insulin was predicted for experiments with either human islets or SC-β cells.

Chip Priming and Insulin Calibration.: Chip experiments were performed on a Leica DMI6000B microscope (Leica Microsystems Inc., Buffalo Grove, IL) with a Tokai Hit STRF-DMIWX-SET stage-top incubator and perfusion block (Tokai Hit., Co, Ltd., Fujinomiya, Shizuoka, Japan) set to 37°C. Chip reservoirs were connected to an OB1 Elveflow Mk3+ pressure regulator (ELVESYS, Paris, France) with 0–2 bar range on each of the 4 channels (ELVESYS, Paris, France). An Elveflow MFS1 flow sensor was in-line with the reservoirs leading to the glucose and islet inlets. PEEK tubing with a 25 μm internal diameter was connected in line with the reagent tubing to lower the flow rate for the operating range of the pump. The chip and tubing were primed and sterilized with 40% ethanol. After priming, reservoirs were filled with solutions for insulin calibration: KRB with 20 mM glucose and 75 mIU/mL human insulin (Sigma-Aldrich, Cat. # I9278) leading to the islet inlet, KRB with 20 mM glucose for the glucose inlet, KRB with 1.6 μM of FITC-insulin (Sigma-Aldrich, Cat. #I3661) connected to the FITC-insulin inlet, and KRB with 1.6 μM of insulin antibody (Meridian Life Science, Inc., Memphis, TN, Cat #E86211M) for the antibody inlet. Once the tubing connecting reservoirs to the chip were filled with their respective solutions, pressures corresponding to a flow rate of 0.1 μL/min were set for the reagents and the islet and glucose inlet reservoirs were set to a combined flow rate of 1.4 uL/min that delivered 40 mIU/mL insulin. After at least an hour of equilibration, flow rates from the islet and glucose inlets were adjusted without changing the combined flow rate to deliver step curves of insulin concentrations between 5 and 65 mIU/mL, each step lasting for 30–45 minutes. After calibration, the insulin solution in the islet reservoir was replaced with

KRB with 2.8 mM glucose and 17.2 mM sucrose (so glucose concentration could be varied independent of osmolarity) and alternating 45-minute steps of 2.8 mM and 20 mM glucose were delivered to flush insulin from the system and to record background traces. After several hours, the reservoir with low glucose was swapped out for one containing a solution of 30 mM KCl to obtain a background recording from this solution as well.

Islet Loading and Glucose Stimulation.: Before priming, the islet inlet was connected to a T-junction tubing connector downstream of the flow sensor. An additional reservoir for cell loading was installed at the top of the T-junction. For islet loading, a hydraulic head was created based on the heights of media in the islet and waste reservoirs. Flow settings on the regulator were not changed during loading. 20–40 islets suspended in KRB with 2.8 mM glucose were added by pipet to the cell loading reservoir and tracked through the chip by microscopy and video recording using a 10x objective and the PCO AG camera listed above (see Parallel flow). Islet diameters were obtained by video analysis and used to convert islet number to IEQ using a reference table from the Integrated Islet Distribution Program (IIDP). After loading, KRB with 2.8 mM and 20 mM glucose was delivered to islets on the chip for in alternating 45 minutes treatments, followed by 45 minutes of KRB containing 30 mM KCl. Cells were maintained in perifusion on the chip for at least 6 hours. Islets from the same isolation were also loaded into a Biorep perifusion system (Biorep, Miami Lakes, FL) in triplicates and perifused at a flow rate of 0.1 mL/min with a one hour fast at 2.8 mM glucose, and then 15 minutes of 2.8 mM glucose, 30 minutes of 20 mM glucose, 15 minutes of 2.8 mM glucose, and finally 15 minutes of 30 mM KCl. Samples were collected at 2-minute intervals and insulin was quantified using an Alpco Ultrasensitive Human Insulin ELISA kit. Insulin concentrations from the perifusion assay were normalized to IEQ using viable cell number and an estimate of 1560 cells per IEQ [37], then converted to secretion rates using the flow rate during perifusion (0.1 mL/min).

Fluorescence Anisotropy Data Acquisition and Analysis.: Measurements were taken using a Leica N Plan 40X/0.64 NA non-polarizing objective and a Lumencor Retra LED light engine (Lumencor, Inc., Beaverton, OR) with a bandpass filter of 475/34 nm. Excitation light was polarized with a Chroma 21003a linear polarizer (Chroma Technology Corp., Bellows Falls, VT) mounted into a Leica 91024 filter cube that also contained a Chroma T495lpxr dichroic mirror and a Chroma 525/50m emission filter. The field diaphragm was set to a circular opening of size 2. Parallel and perpendicular components of fluorescent emissions were separated using a Thorlabs CM1-PBS251 polarizing beam splitter (Thorlabs, Newton, New Jersey) that was aligned at right angles (within 1 degree) with the light path using a protractor. Emissions were quantified by Hamamatsu H10722–01 photomultiplier tubes (PMT) connected to each branch of the beam splitter. Each PMT was provided +5/−5 V by an Agilent power supply and was wired into a D-sub connector that attached to a custom printed circuit board (PCB) containing a low-pass RC filter with a 330 μF capacitor and a potentiometer to attenuate noise in the signal channel of 0.8 Hz or higher. PMTs were connected to a National Instruments USB6009 data acquisition card (National Instruments, Woburn, MA) using another D-sub connector plugged into the PCB. PMT voltages and timestamps were recorded with desired PMT gain and sampling frequency using a custom LABVIEW (National Instruments) interface that also controlled the intensity of excitation light from the light engine. Recordings were primarily conducted with control voltages of 0.6–0.7 V for both PMTs, light intensity of 15%, and a sampling frequency of 1 Hz. A custom MATLAB script was used to calculate fluorescence anisotropy, r, from recorded voltages as:

$$r = \frac{V_{\parallel} - V_{\perp}}{V_{\parallel} + 2V_{\perp}} \tag{9}$$

where $V_{\parallel}$ is the PMT voltage from the parallel component and $V_{\perp}$ is the PMT voltage from the perpendicular component. For insulin calibrations, another MATLAB script also calculated insulin concentrations using flow sensor data for comparison with average anisotropy shifts (relative to the anisotropy measured for 0 mIU/mL insulin) measured during each calibration step. Fluorescence anisotropy values corresponding to 0 mIU/mL insulin were extrapolated in cases where that data point was not obtained. Individual calibration experiments were normalized for aggregation using the anisotropy shift at saturation. A four-parameter logistic fit was applied to the aggregated calibration data, as described by the equation:

$$\Delta r = \frac{D + (A - D)}{1 + \left(\frac{I^{B}}{C}\right)} \tag{10}$$

where Δr is the anisotropy shift, I is the insulin concentration, A is the minimum asymptote, B is the Hill slope, C is the inflection point, and D is the maximum asymptote. Using a modified version of a logistic fit algorithm written in MATLAB [38], the calibration curve in Figure 7b was obtained, with A, B, C, and D values of −9.734, −1.359, 8.294, and −0.02757, respectively, and an R^2 value of 0.9346. To quantify insulin secreted from islets, raw anisotropies were background corrected and converted to insulin concentrations using the aggregated calibration curve. For background correction, a section of a glucose trace taken prior to cell loading was overlaid temporally with the islet anisotropy recording, and then the anisotropy was subtracted out. Secretion rates were calculated from insulin concentrations by multiplying by the flow rate and dividing by IEQ.

Results and Discussion

Device Design and Fabrication.

To design the Islet on a Chip, we synthesized feedback from potential users and compiled a list of device design criteria (Table 1)[39]. Desired criteria included scalable manufacturing (moldable materials), ease of use (one-piece chip, automation), insulin sensing capabilities (continuous readout), and homogeneous microenvironments supporting islet viability (parallel flow, oxygenation). The latter consideration was inspired by the parallel vascularization of islets *in vivo*, where islets have 1–3 designated arterioles [40] (Figure 1a). A survey of previously published microfluidic devices for measuring insulin secretion indicated that none fully satisfied these design criteria (Table 2). Thus, our approach was to enforce a high degree of spatial and temporal stimulus control for functional potency testing of islets, while maintaining scalability and user-friendliness. Figures 1b and 1c display how we implemented these design goals into one system. Our single-piece chip features four main motifs. First, the islet and glucose inlets introduce two solutions that can be mixed in different ratios for dynamic inputs. Such an approach is useful for delivering intermediate concentrations of glucose from solutions of low and high glucose. Second, the culture region contains sixteen islet traps set in parallel channels with equivalent flow resistances and path lengths. Islets introduced to the chip from the islet inlet are automatically captured in the traps. After the traps have been filled during loading, excess islets exit the chip via the islet shunt so they can be used for other assays. Third, the chip has sequential inlets and mixing channels for adding reagents to the perfusate to enable insulin sensing. After each inlet, channels are organized into serpentine motifs to provide sufficient length for diffusional mixing while compacting the overall chip footprint. Finally, the chip contains a glass capillary for optical sensing of insulin. The capillary forms a continuous part of the flow path and is suspended in an opening that accommodates a standard microscope objective. The main outlet after the capillary is for waste removal.

To achieve the goal of scalable manufacturing, we selected polycarbonate as the primary device material. While glass [13–16,16–22,41] and polydimethylsiloxane (PDMS) [8,10–12,23,28,42–49] are frequently used for microfluidic device fabrication, PDMS alters reagent delivery through absorption of lipophilic compounds [50,51] such as steroid hormones [52] and multiple drugs [53]. Polycarbonate is less prone to drug absorption than PDMS [53] and unlike glass is compatible with safer commercial fabrication methods. Our device was created across two polycarbonate layers using a Computer Numerical Control (CNC) mill (Figure 3a). Islet traps were formed by constricting channel width from 400 to 75 μm (Figure 3b). While smaller end mills can produce features as small as 4 μm [54], each half of each islet trap was milled on opposite layers to provide clearance for larger, more robust end mills. Enabled by their unique fabrication method, the traps also have 75 μm deep shelves cut away either above or below each half to allow additional flow through the trap even when an islet is present (Figure 3b). For integration of the capillary into the polycarbonate chip, a gasket was first applied to either end of the capillary before placing the ends of the capillary into glands on each of the two chip layers prior to bonding [55].

To build the chip, we used standard thermoplastic fabrication protocols (Figure 3c). After milling, layers were post-processed by removing excess material, sanding the faces to achieve a flat surface, and cleaning with isopropanol to clear away residue. Each layer was then vapor polished for optical clarity and a smoothed finish. Once polished, chip components were assembled and placed between two glass panes to preserve the smooth finish during bonding. Alignment between the two layers was accomplished through a combination of alignment posts and holes on the top and bottom layers, respectively. The capillary sandwiched between the chip layers also provided a significant contribution to alignment, primarily through its gasket glands (Figure 3a). Gasket glands on each layer were dimensioned such that the diameter of the glands was less than the diameter of the gaskets, ensuring that when the capillary with gaskets on either end was placed in between the two layers it would also provide a strong centering force from the elasticity of the gaskets pushing equally along the circumference of the gland. This assembly was itself placed between sheets of silicone within a hydraulic press, the silicone affording some degree of force redistribution to account for unevenness in the press surfaces. The chip was then bonded into a single piece using a combination of pressure and heat near the glass transition temperature. Each chip was inspected for proper trap alignment under a microscope both before and after bonding. A chip was considered unusable if even one channel was occluded due to trap misalignment. We obtained a failure rate of around 10% in fabrication due to misaligned traps, which was the most common issue leading to chip failure. In addition to trap formation, chips were also inspected for a broken or mis-aligned capillary. Chips with a full complement of open traps were then fluid tested to ensure proper fluid flow. While uncommon, trap alignment could be addressed through more repeatable manufacturing approaches. The current method of fabrication uses CNC milling, but feature dimensions in the chip are compatible with hot embossing or injection molding [56], which can improve the throughput and consistency of production.

Hydrodynamic Trapping of Islets.

The islet trapping feature in the device (Figure 4a) adds convenience both by automating the loading process and, when flow is reversed, by facilitating islet recovery for offline analysis after experiments on the device. Moreover, the defined position of islets eliminates search time for islet imaging experiments and inherently creates a more predictable microenvironment around islets, as in other trap devices [8,11,12,44,47,49,57–59] Automatic loading in our device was achieved by taking advantage of the inherent increase in flow resistance through a trap after islet capture. The resistance increase in occupied traps redirects flow – and islets carried by the flow – toward vacant traps. To estimate the resistance increase after islet capture, we used a computational fluid dynamics model to predict the pressure across occupied versus vacant traps (Figure 4b) and converted pressure to resistance (Eqns. 1–3; see Materials and Methods). Since cadaveric islet preparations contain a range of islet sizes (~50–500 μm in diameter), trap width was set to 75 μm to select for larger islets that would have a greater impact on trap resistance and thus decrease the chance of capturing two islets in a single trap. To automatically direct excess islets to the islet shunt when all traps are occupied, resistance in the islet shunt was designed to be much less than the trapping region when fully occupied but still greater than a vacant trap. After all untrapped islets exited the device, a stopcock connected to the islet outlet would be closed to direct all upstream flow toward the trapping region. Similarly, we modeled oxygenation and shear forces (Eqn. 4; see Materials and Methods) around captured islets to select flow rates that would provide sufficient oxygen without damaging islets (Figure 4c). Calculated oxygen delivery for each trap was sufficient for more than six 150 μm diameter islets, while predicted shear values were several orders of magnitude less than the average reported stiffness of the tissue [60], and thus not expected to deform trapped islets to any meaningful degree. Shear values were also well below those previously suggested to be acceptable for islet culture [~6 mPa [57]]. Collectively, the trapping design offered a robust approach for spatially organizing the islets in an automated fashion while providing a physiologically-relevant environment.

We tested the trapping device by tracking capture events during islet loading. Consistent with our model, we observed automatic capture of islets in parallel channels (Figure 4d) as well as the escape of smaller islets through the traps. To determine the size threshold for islet capture, we extracted islet diameter information during trapping or escape events and plotted trapping frequency as a function of islet size (Figure 4e). We observed a clear difference in the distributions of islet size between islets that escaped versus those that were captured by a vacant trap ($p = 1.2 \times 10^{-11}$; n = 53 islets; $D = .969$; two-sample Kolmogorov-Smirnov test), with all islets less than 150 μm in diameter escaping, all islets greater than 180 μm in diameter being captured, and two out of three islets between 150 and 180 μm in diameter also being captured. Next, we quantified the number of islet capture events per trap (Movie S1). On average, 1.5 ± 0.2 islets or islet clusters (n = 39 capture events in 26 traps observed live for two separate experiments, standard error) were captured per trap, which was comparable to the predicted value (1.5 islets per trap) that we obtained from 10,000 *in silico* loading experiments (see Materials and Methods). Since captured islet size is positively associated with trap resistance, the probability of capturing multiple islets in a single trap is higher for traps occupied by smaller islets (Figure S1). Moreover, this probability naturally increases as traps are filled. Additional design elements or experimental procedures could be implemented to increase the probability of capturing a single islet in all traps. Altogether, these results demonstrated the ability of the device to automatically capture islets in parallel traps and delineated a minimum size threshold (150 μm islet diameter for 75 μm trap openings) for islet capture.

Synchronized Perifusion of Islets with Dynamic Glucose Stimulation.

A limitation of traditional well-based platforms – or even many microfluidic devices [8,11,12,14,44,47–49,61] – is that individual islets do not have a designated nutrient supply, leading to heterogeneity in the oxygenation, nutrient content, stimulation, and feedback mechanisms based on the number and proximity of their neighbors. In addition to its biomimetic nature, application of parallel delivery overcomes this major limitation by providing a consistent microenvironment for all islets in the device and by synchronizing introduced stimuli. To enable parallel stimulus delivery on our chip, the channel that connects the islet and glucose inlets to the islet traps has four nested, symmetrical branches. Before fabrication, we tested the design by simulating the delivery of a glucose step function to a two-dimensional projection of the chip (Figure 5a). Changes to steady-state glucose concentrations were made by adjusting relative flow rates from the opposing inlets. The overall duration (~2 hours) and dynamic range (5 to 8 mM) of the step function were comparable to postprandial glucose dynamics in humans [62]. The simulated input (Figure 5b) was preserved downstream at separate traps, which mirrored one another both in timing and magnitude (Figure 5c–d). We then validated the simulation empirically by delivering a ten-minute pulse of fluorescent glucose to a device loaded with human islets (Figure 5e–g and Movie S2; see Materials and Methods). We assessed stimulus synchronization under conditions with the largest possible differences in theoretical resistance, from a vacant trap

(Channel 4 in Figure 5g) to an islet filling the entire channel width (Channel 2 in Figure 5g). A trap filled by three islets (Channel 5 in Figure 5g) was also represented in our experiment. By analyzing fluorescence intensity across traps during a time course (Figure 5h), we observed that stimulus intensities were similar (91 ± 3% of maximum; standard error; Figure 5i), indicating that the concentrations of glucose delivered to islets were consistent. Moreover, both the onsets (Figure 5j) and durations (Figure 5k) of the stimulus were synchronized across all the traps within two minutes of each other. Taken together, the results demonstrated that our parallel channel design synchronized stimulus delivery and provided a consistent microenvironment around each islet in the chip.

Insulin Sensing by an On-chip Insulin Immunoassay Quantified by Fluorescence Anisotropy.

One main advantage of microfluidics is realized by miniaturizing functional assays and thus minimizing the required volumes of assay reagents. By comparison with ELISA, the insulin immunoassay[13–24,63] in the Islet on a Chip reduces the minimum sample volume by orders of magnitude, allowing more measurements per volume of reagent in a continuous manner (Table 3). The immunoassay utilizes fixed amounts of fluorophore-tagged insulin (FITC-insulin) to compete with unlabelled antigen in the islet secretions for antibody binding (Figure S2a). FITC-insulin and insulin antibody are flowed into the chip downstream of the trap region and must be evenly mixed into the flow for the continuous detection of insulin at the capillary (Figure S2b–c). Channel lengths required for complete mixing of both insulin and insulin antibody were calculated based on the channel width, flow rate, and diffusion constants of each species (Eqns. 5–7; see Materials and Methods). Since we did not find literature values, we estimated the diffusion constants for insulin antibody and FITC-insulin with the Stokes-Einstein relation to be 2.8×10^{-11} m^2/s and 10.9×10^{-11} m^2/s, respectively (Eqn. 8; see Materials and Methods). We then quantified reagent mixing empirically for both reagents by tracking FITC-insulin and a secondary antibody throughout the mixing channels by fluorescence microscopy (Figure S2d). Image analysis confirmed uniform concentrations of each across the width of the channel before entering the capillary (Figure S2e–f).

Within the capillary, the immunoassay is quantified by monitoring fluorescence anisotropy of FITC-insulin, as we have done previously with Cy5-insulin [63] to measure insulin secretion from mouse islets [15]. When a fluorescent molecule is excited with a polarized light source, the fluorescence anisotropy measures the amount of emitted light that is parallel to the incident light as compared to the total light emitted [64] (Figure 6a; Eqn. 9; see Materials and Methods). In our implementation, fluorescence anisotropy of FITC-insulin was modulated by antibody binding, which decreased the molecular rotation of the fluorophore and made it more likely to maintain its initial polarization state during the fluorescence lifetime. Furthermore, in the presence of secreted insulin, a portion of the FITC-insulin is unable to bind to the antibody, leaving it free to rotate more quickly. As a result, the fraction of FITC-insulin bound by the antibody is inversely proportional to the amount of insulin secreted and can be quantified by changes in fluorescence anisotropy (Figure 6b). To conduct measurements of fluorescence anisotropy, we utilized a traditional epifluorescence microscopy light path containing a linear polarizer to align the light prior to hitting the sample and a polarizing beam splitter to separate the parallel and perpendicular components for quantification (Figure 6c). We also mounted our chip into an on-stage incubator for temperature control (Figure 6d). An overall view of our sensing equipment is shown in Figure 6e. We next flowed insulin solutions through the device (Figure 6f), including concentrations that were predicted to be produced by islets in the chip (1–30 mlU/mL; see Materials and Methods). While ELISA is more sensitive for insulin detection, the assay typically requires a minimum sample volume of 25 μL, three orders of magnitude higher than the amount of fluid being analysed at any given moment on the Islet on a Chip. By selecting a flow rate that concentrated insulin secretions to detectable quantities based on average basal and glucose stimulated secretion rate, we obtained a comparable dynamic range for insulin detection (Table 3). With increasing concentrations of insulin to fixed amounts of FITC-insulin and insulin antibody, we observed a decrease in anisotropy. The condition without any insulin present in a mixture of FITC-insulin and insulin antibody produced the theoretical maximum anisotropy for the immunoassay, and the highest concentrations of insulin produced the same anisotropy value as a solution of FITC-insulin by itself, the theoretical minimum anisotropy. Anisotropy values returned to baseline after removal of insulin from the system, demonstrating that we could expect to measure both increasing and decreasing changes in insulin level. We demonstrated that the sensor could measure dynamic anisotropy and that its insulin detection capabilities include the secretion rates of human islets.

Quantifying Insulin Secretion Rates of Stimulated Human Islets by On-chip Insulin Sensing.

Having shown the ability of our device to trap islets, deliver parallel flow, and measure insulin concentration, we were able to investigate the insulin response from human islets to glucose pulses on the chip. Figure 7a outlines the basic sequence for an islet experiment. For our on-chip insulin calibrations, we delivered insulin from the islet inlet and combined it with a solution without insulin from the glucose inlet. Adjusting the fraction of total flow from each inlet allowed us to deliver step curves of insulin concentrations to the chip. Simultaneously, we maintained concentrations of FITC-insulin and insulin antibody. The islet outlet was closed to allow for all flow to pass through the capillary for measurement. Because fluorescence anisotropy values were sensitive to the amount of glucose in the system, we swapped the solution at the islet inlet to 2.8 mM glucose after insulin calibration and conducted a negative control glucose stimulation protocol without cells, which was later used to correct for background noise in the human islet trace (Figure S3). We then opened the islet outlet and introduced human cadaveric islets through the islet inlet. Since we did not size select the islets that were loaded, some traps captured multiple islets [43 islets or 64 islet equivalents (IEQ) were captured in total] as discussed above (see Hydrodynamic Trapping of Islets*).* The islet outlet was closed after excess islets were flushed from the system and islets were perifused with islet assay buffer with 2.8 mM glucose for 4 hours. We then delivered 45-minute steps of 2.8 mM and 20 mM glucose to the captured islets, while recording the fluorescence anisotropy at the capillary. After islets had been perifused for 6 hours, they were also treated with a 30 mM KCl solution as a positive control for insulin secretion. For comparison, islets from the same isolation were also stimulated in a similar manner using a standard perifusion system (see Islet Loading and Glucose Stimulation*).*

To convert between anisotropy measurements and insulin concentrations, we aggregated calibration curves from four different recordings (n = 9 calibrations) (Figure 7b; Eqn. 10; see Materials and Methods). While calibrations performed during the same experiment were reproducible, the dynamic range of anisotropy changes varied between calibrations performed on different days. The aggregated calibration curve was therefore scaled by the dynamic range of anisotropy changes measured on the same day that insulin secretion was measured. Before converting to insulin concentration, the fluorescent anisotropy trace was corrected using a background trace recorded before cells were loaded (Figure S3, see Materials and Methods). Given the flow rate within the chip, concentrations were converted into secretion rates and normalized to IEQ to control for the effect of islet size on insulin secretion [65] (see Materials and Methods). Upon stimulation with both 20 mM glucose and 30 mM KCl, we observed peaks (0.20.3 μIU/min*IEQ) above background levels that fall within reported insulin secretion values during stimulation [30,66,67] (Figure 7c). Since the KCl recording followed perifusion of the islets for at least 6 hours, we also demonstrated that longer stimulation protocols are feasible. During this time, thousands of continuous insulin measurements were made, which would require dozens of ELISA plates to obtain the same amount of data. The on-chip responses appeared to match the form of those from the conventional perifusion method. We did observe that the peaks were lower in the Islet on a Chip recordings compared to the standard perifusion assay, which is perhaps attributable to the additional day islets were in culture prior to the former experiment compared to the latter. This observation may also likely be a result of diffusion during on-chip mixing steps. Diffusional broadening can be diminished by decreasing channel dimensions or resolved with deconvolution analysis. Overall, the continuous measurement of insulin secreted from human islets stimulated by synchronized pulses of glucose represents an important demonstration of principle for islet potency testing using this technology.

We performed additional tests to confirm that islets on the chip were sufficiently oxygenated and viable after loading and on-chip stimulation. Media delivered to the chip was equilibrated with atmospheric oxygen at pressures just above 1 atm. Using a dye that generates fluorescent metabolites under hypoxic conditions, we tracked islet oxygenation over the course of glucose stimulation on the chip (Figure S4). Fluorescence within islets on the chip in both low and high glucose was weak and comparable to islets maintained in static culture. By contrast, islets that were stained immediately after shipping exhibited a strong fluorescent signal likely due to cold ischemia (Figure S4f). These results indicate sufficient oxygenation on the chip. As a final test of the chip, we measured cell survival. By introducing backflow, all islets could be recovered intact from the chip after several hours of perifusion. Staining recovered islets with propidium iodide demonstrated that islets survived chip loading, glucose stimulation, and recovery as evidenced by propidium iodide exclusion (Figure S5). Together, these studies indicate that culture conditions on the chip did not contribute to a measurable disruption to oxygenation or viability as compared to static culture.

Having shown that the Islet on a Chip can measure dynamic insulin secretion from human islets, what remains to be done to facilitate its use in practice? A meta-analysis of human islet research highlighted significant functional variability between islet isolations, for reasons independent of factors such as isolation center, biological data, or isolation technique[68]. Such findings underscore the need for additional research to identify variables corresponding most to islet function and that are predictive of transplantation success. One fundamental question pertains to the appropriate sample size of islets needed to adequately assess islet function. While some have utilized triplicates of 15 islets for assessing function of islet isolations[69], similar comparative work has also used 60 to 100 islets, or variable amounts of islets whose output was normalized to total insulin content[70,71]. All cases were impressive in scope and informative of the challenges in the current state of human islet research, but did not comment specifically on the sample size needed to account for the average function of an entire islet preparation. Recently, the Hara group estimated that 400 islets would need to be sampled from a pancreas to arrive at a reasonable estimate for the population mean for β cell proportion[72]. Whether this sample size also adequately accounts for the function of an islet preparation remains unknown. The Islet on a Chip described here may aid in the exploration of this essential question, by allowing for continued study of the dynamic function of islets from different isolations. Since the design is modular and chip fabrication scalable, the number of traps on the chip can be altered to offer functional testing of a larger pool of islets. Beyond defining experimental parameters for islet potency testing, there are additional capabilities that would enhance the accessibility of the platform. While the device already affords distinct advantages over ELISA (Table 3) by automating much of the operation relative to previous microfluidic devices (Table 2), additional automation would ease the burden of adopting the Islet on a Chip platform. For example, in this study fluorescence anisotropy measurements were made using a custom microscope. Development of a portable, dedicated reader with integrated microfluidic flow control would eliminate the need for users to acquire and install individual equipment components, which represents a significant barrier to adoption. As more members of the islet field begin to use this technology, we anticipate that it can help standardize and increase the predictive utility of islet testing.

Conclusions

The Islet on a Chip is distinguished by the combination of scalable construction, synchronized islet stimulation, and the automation of every aspect of functional testing from islet loading to insulin measurement. A continuous readout generates data with time resolution superior to what is feasible for experiments using commercial ELISAs and potentiates analysis of secretion dynamics from isolated islets. Beyond glucose, islet responses to other physiologically-relevant stimuli such as incretins, glucagon, or amino acids could also be interrogated on the device. Individual features such as the size of the trap opening can be customized based on the intended application. Given that some experimentalists may want to query the full range of sizes in human islet preparations, on-chip motifs for automatic size sorting [73] could also be included in combination with a gradient of trap sizes. Capturing a range of islet sizes would also reduce the bias of islet size on islet cell composition[74]. By altering the number of branches in the design and adjusting the total flow rate accordingly, one can select the number of islets for parallel stimulation. Moreover, individual channels can be extended downstream of the traps to enable parallel sensing of separate islets. Vasculature could be also integrated to more closely mimic physiological nutrient delivery to islets, although the time required for vascularizing islets in vitro limits its utility for donor islet testing. Altogether, the work helps bridge the broader islet community with the powerful technologies that microfluidics affords for islet testing and provides an agile, scalable device for diabetes research.

Supplementary Material

Refer to Web version on PubMed Central for supplementary material.

Acknowledgement

We thank M. Rosnach for photographs and illustrations, A. McClelland for help with optics assembly, D. Drennan for building the sensor case, H. Ardoña for freeze-drying reagents, L. Scudder for sharing buffers, J. MacArthur for loaning the power supply, Q. Peterson and A. Gannon for suggestions with earlier chip versions, Elise Engquist for help making insulin-free media, and Joel Adablah for advice on fluidic connections. B.D.P. is a Good Ventures Fellow of the Life Sciences Research Foundation. National Institute of Diabetes and Digestive and Kidney Diseases awards UC4 DK104165 to D.A.M. and K.K.P. and UC4 DK116283 and RO1 DK080714 to M.G.R, Harvard Materials Research Science and Engineering Centers (grant no. DMR- 1420570), and Harvard Center for Nanoscale Systems (a member of the National Nanotechnology Infrastructure Network) under NSF award 1541959 supported the work.

Notes and References

1. Banting FG and Best CH, I Lab. Clin. Med, 1922, 7, 251–266.
2. Sneddon JB, Tang Q, Stock P, Bluestone JA, Roy S, Desai T. and Hebrok M, Cell Stem Cell, 2018, 22, 810–823. [PubMed: 29859172]
3. Ricordi C, Goldstein JS, Balamurugan AN, Szot GL, Kin T, Liu C, Czarniecki CW, Barbaro B, Bridges ND, Cano J, Clarke WR, Eggerman TL, Hunsicker LG, Kaufman DB, Khan A, Lafontant D-E, Linetsky E, Luo X, Markmann JF, Naji A, Korsgren O, Oberholzer J, Turgeon NA, Brandhorst D, Chen X, Friberg AS, Lei J, Wang L-J, Wilhelm JJ, Willits J, Zhang X, Hering BJ, Posselt AM, Stock PG, Shapiro AMJ and Chen X, Diabetes, 2016, 65, 3418–3428. [PubMed: 27465220]
4. Untereiner A, Abdo S, Bhattacharjee A, Gohil H, Pourasgari F, Ibeh N, Lai M, Batchuluun B, Wong A, Khuu N, Liu Y, Al Rijjal D, Winegarden N, Virtanen C, Orser BA, Cabrera O, Varga G, Rocheleau J, Dai FF and Wheeler MB, FASEB J. Off. Publ. Fed. Am. Soc. Exp. Biol, 2018, fj201801397R.
5. Wan X, Zinselmeyer BH, Zakharov PN, Vomund AN, Taniguchi R, Santambrogio L, Anderson MS, Lichti CF and Unanue ER, Nature, 2018, 560, 107–111. [PubMed: 30022165]
6. Wang Y, Lo JF, Mendoza-Elias JE, Adewola AF, Harvat TA, Kinzer KP, Lee D, Qi M, Eddington DT and Oberholzer J, Bioanalysis, 2010, 2, 1729–1744. [PubMed: 21083325]
7. Castiello FR, Heileman K. and Tabrizian M, Lab. Chip, 2016, 16, 409–431. [PubMed: 26732665]
8. Heileman K, Daoud J, Hasilo C, Gasparrini M, Paraskevas S. and Tabrizian M, Biomicrofluidics, 2015, 9, 044125.
9. Lam AK, Silva PN, Altamentova SM and Rocheleau JV, Integr. Biol, 2012, 4, 838.
10. Chen W, Lisowski M, Khalil G, Sweet IR and Shen AQ, PloS One, 2012, 7, e33070.
11. Adewola AF, Lee D, Harvat T, Mohammed J, Eddington DT, Oberholzer J. and Wang Y, Biomed. Microdevices, 2010, 12, 409–417. [PubMed: 20300858]
12. Lee D, Wang Y, Mendoza-Elias JE, Adewola AF, Harvat TA, Kinzer K, Gutierrez D, Qi M, Eddington DT and Oberholzer J, Biomed. Microdevices, 2012, 14, 7–16. [PubMed: 21850483]
13. Dishinger JF, Reid KR and Kennedy RT, Anal. Chem, 2009, 81, 3119–3127. [PubMed: 19364142]
14. Yi L, Wang X, Dhumpa R, Schrell AM, Mukhitov N. and Roper MG, Lab. Chip, 2015, 15, 823–832. [PubMed: 25474044]
15. Schrell AM, Mukhitov N, Yi L, Adablah JE, Menezes J. and Roper MG, Anal Methods, 2017, 9, 38–45. [PubMed: 28458724]
16. Roper MG, Shackman JG, Dahlgren GM and Kennedy RT, Anal. Chem, 2003, 75, 4711–4717. [PubMed: 14674445]

17. Lu S, Dugan CE and Kennedy RT, Anal. Chem, 2018, 90, 5171–5178. [PubMed: 29578696]
18. Bandak B, Yi L. and Roper MG, Lab. Chip, 2018, 18, 2873–2882. [PubMed: 30109329]
19. Dishinger JF and Kennedy RT, Anal. Chem, 2007, 79, 947–954. [PubMed: 17263320]
20. Shackman JG, Dahlgren GM, Peters JL and Kennedy RT, Lab. Chip, 2005, 5, 56–63. [PubMed: 15616741]
21. Lomasney AR, Yi L. and Roper MG, Anal. Chem, 2013, 85, 7919–7925. [PubMed: 23848226]
22. Reid KR and Kennedy RT, Anal. Chem, 2009, 81, 6837–6842. [PubMed: 19621896]
23. Chen D, Du W, Liu Y, Liu W, Kuznetsov A, Mendez FE, Philipson LH and Ismagilov RF, Proc. Natl. Acad. Sci. U. S. A, 2008, 105, 16843–16848. [PubMed: 18974218]
24. Schultz NM, Huang L. and Kennedy RT, Anal. Chem, 1995, 67, 924–929. [PubMed: 7762828]
25. Nunemaker CS, Dishinger JF, Dula SB, Wu R, Merrins MJ, Reid KR, Sherman A, Kennedy RT and Satin LS, PloS One, 2009, 4, e8428.
26. Wang Y, Lee D, Zhang L, Jeon H, Mendoza-Elias JE, Harvat TA, Hassan SZ, Zhou A, Eddington DT and Oberholzer J, Biomed. Microdevices, 2012, 14, 419–426. [PubMed: 22252566]
27. Sankar KS, Green BJ, Crocker AR, Verity JE, Altamentova SM and Rocheleau JV, PloS One, 2011, 6, e24904.
28. Godwin LA, Pilkerton ME, Deal KS, Wanders D, Judd RL and Easley CJ, Anal. Chem, 2011, 83, 7166–7172. [PubMed: 21806019]
29. Zhang X, Grimley A, Bertram R. and Roper MG, Anal. Chem, 2010, 82, 6704–6711. [PubMed: 20617825]
30. Pagliuca FW, Millman JR, Gürtler M, Segel M, Van Dervort A, Ryu JH, Peterson QP, Greiner D. and Melton DA, Cell, 2014, 159, 428–439. [PubMed: 25303535]
31. Tziampazis E. and Sambanis A, Biotechnol. Prog, 1995, 11, 115–126. [PubMed: 7766095]
32. Shorten PR, McMahon CD and Soboleva TK, Biophys. J, 2007, 93, 3001–3007. [PubMed: 17631540]
33. Thomas GD, Drug Target, 2000, 25, 115–132.
34. Jampol LM and Cunha-Vaz J, in Pharmacology of the Eye, ed. Sears ML, Springer Berlin Heidelberg, Berlin, Heidelberg, 1984, vol. 69, pp. 699–714.
35. Buchwald P, Theor. Biol. Med. Model, 2011, 8, 1–25. [PubMed: 21247471]
36. Wenger R, Kurtcuoglu V, Scholz C, Marti H. and Hoogewijs D, Hypoxia, 2015, 3, 35. [PubMed: 27774480]
37. Pisania A, Weir GC, O'Neil JJ, Omer A, Tchipashvili V, Lei J, Colton CK and Bonner-Weir S, Lab. Invest, 2010, 90, 1661–1675. [PubMed: 20697378]
38. Cardillo G, Four parameters logistic regression - There and back again, https://it.mathworks.com/matlabcentral/fileexchange/38122, (accessed February 22, 2019).
39. Capulli AK, Tian K, Mehandru N, Bukhta A, Choudhury SF, Suchyta M. and Parker KK, Lab. Chip, 2014, 14, 3181. [PubMed: 24828385]
40. Jansson L, Barbu A, Bodin B, Drott CJ, Espes D, Gao X, Grapensparr L, Källskog Ö, Lau J, Liljebäck H, Palm F, Quach M, Sandberg M, Strömberg V, Ullsten S. and Carlsson P-O, Ups. J. Med. Sci, 2016, 121, 81–95. [PubMed: 27124642]
41. Li PC and Harrison DJ, Anal. Chem, 1997, 69, 1564–1568. [PubMed: 9109354]
42. Rocheleau JV, Walker GM, Head WS, McGuinness OP and Piston DW, Proc. Natl. Acad. Sci. U. S. A, 2004, 101, 12899–12903. [PubMed: 15317941]
43. Easley CJ, Rocheleau JV, Head WS and Piston DW, Anal. Chem, 2009, 81, 9086–9095. [PubMed: 19874061]
44. Mohammed JS, Wang Y, Harvat TA, Oberholzer J. and Eddington DT, Lab. Chip, 2009, 9, 97–106. [PubMed: 19209341]
45. Duffy DC, McDonald JC, Schueller OJ and Whitesides GM, Anal. Chem, 1998, 70, 4974–4984. [PubMed: 21644679]
46. Delamarche E, Bernard A, Schmid H, Michel B. and Biebuyck H, Science, 1997, 276, 779–781. [PubMed: 9115199]

47. Xing Y, Nourmohammadzadeh M, Elias JEM, Chan M, Chen Z, McGarrigle JJ, Oberholzer J. and Wang Y, Biomed. Microdevices, 2016, 18, 80. [PubMed: 27534648]
48. Li X, Brooks JC, Hu J, Ford KI and Easley CJ, Lab. Chip, 2017, 17, 341–349. [PubMed: 27990542]
49. Lo JF, Wang Y, Blake A, Yu G, Harvat TA, Jeon H, Oberholzer J. and Eddington DT, Anal. Chem, 2012, 84, 1987–1993. [PubMed: 22296179]
50. Adiraj Iyer M. and Eddington DT, Lab. Chip, 2019, 19, 574–579. [PubMed: 30681692]
51. Minagawa T, Kohno Y, Suwa T. and Tsuji A, Pharm. Res, 1994, 11, 503–507. [PubMed: 8058605]
52. Regehr KJ, Domenech M, Koepsel JT, Carver KC, Ellison-Zelski SJ, Murphy WL, Schuler LA, Alarid ET and Beebe DJ, Lab. Chip, 2009, 9, 2132–2139. [PubMed: 19606288]
53. van Meer BJ, de Vries H, Firth KSA, van Weerd J, Tertoolen LGJ, Karperien HBJ, Jonkheijm P, Denning C, IJzerman AP and Mummery CL, Biochem. Biophys. Res. Commun, 2017, 482, 323–328. [PubMed: 27856254]
54. Kirsch Benjamin, Bohley Martin, Arrabiyeh Peter and Aurich Jan, Micromachines, 2017, 8, 261.
55. Evander M. and Tenje M, J. MicromechanicsMicroengineering, 2014, 24, 027003.
56. Katoh T, Tokuno R, Zhang Y, Abe M, Akita K. and Akamatsu M, Microsyst. Technol, 2008, 14, 1507–1514.
57. Silva PN, Green BJ, Altamentova SM and V Rocheleau J, Lab. Chip, 2013, 13, 4374–84. [PubMed: 24056576]
58. Nourmohammadzadeh M, Lo JF, Bochenek M, Mendoza-Elias JE, Wang Q, Li Z, Zeng L, Qi M, Eddington DT, Oberholzer J. and Wang Y, Anal. Chem, 2013, 85, 11240–11249. [PubMed: 24083835]
59. Nourmohammadzadeh M, Xing Y, Lee JW, Bochenek MA, Mendoza-Elias JE, McGarrigle JJ, Marchese E, Chun-Chieh Y, Eddington DT, Oberholzer J. and Wang Y, Lab. Chip, 2016, 16, 1466–1472. [PubMed: 26999734]
60. Nagy N, de la Zerda A, Kaber G, Johnson PY, Hu KH, Kratochvil MJ, Yadava K, Zhao W, Cui Y, Navarro G, Annes JP, Wight TN, Heilshorn SC, Bollyky PL and Butte MJ, J. Biol. Chem, 2018, 293, 567–578. [PubMed: 29183997]
61. Lenguito G, Chaimov D, Weitz JR, Rodriguez-Diaz R, Rawal SAK, Tamayo-Garcia A, Caicedo A, Stabler CL, Buchwald P. and Agarwal A, Lab. Chip, 2017, 17, 772–781. [PubMed: 28157238]
62. Freckmann G, Hagenlocher S, Baumstark A, Jendrike N, Gillen RC, Rossner K. and Haug C, J. Diabetes Sci. Technol, 2007, 1, 695–703. [PubMed: 19885137]
63. Schrell AM, Mukhitov N. and Roper MG, Anal. Chem, 2016, 88, 7910–7915. [PubMed: 27440478]
64. Jameson DM and Ross JA, Chem. Rev, 2010, 110, 2685–2708. [PubMed: 20232898]
65. Warnock GL, Ellis D, Rajotte RV, Dawidson I, Baekkeskov S. and Egebjerg J, Transplantation, 1988, 45, 957–963. [PubMed: 2835843]
66. Hellman B, Salehi A, Gylfe E, Dansk H. and Grapengiesser E, Endocrinology, 2009, 150, 5334–5340. [PubMed: 19819962]
67. Walker JN, Ramracheya R, Zhang Q, Johnson PRV, Braun M. and Rorsman P, Diabetes Obes. Metab, 2011, 13 Suppl 1, 95–105. [PubMed: 21824262]
68. Hart NJ and Powers AC, Diabetologia, 2019, 62, 212–222. [PubMed: 30547228]
69. Lyon J, Manning Fox JE, Spigelman AF, Kim R, Smith N, O'Gorman D, Kin T, Shapiro AMJ, Rajotte RV and MacDonald PE, Endocrinology, 2016, 157, 560–569. [PubMed: 26653569]
70. Kayton NS, Poffenberger G, Henske J, Dai C, Thompson C, Aramandla R, Shostak A, Nicholson W, Brissova M, Bush WS and Powers AC, Am. J. Physiol. Endocrinol. Metab, 2015, 308, E592–602. [PubMed: 25648831]
71. Henquin J-C, Physiol. Rep, , D0I:10.14814/phy2.13646.
72. Dybala MP and Hara M, Diabetes, , D0I:10.2337/db19-0072.
73. Amini H, Lee W. and Di Carlo D, Lab. Chip, 2014, 14, 2739–2761. [PubMed: 24914632]
74. Kilimnik G, Jo J, Periwal V, Zielinski MC and Hara M, Islets, 2012, 4, 167–172. [PubMed: 22653677]

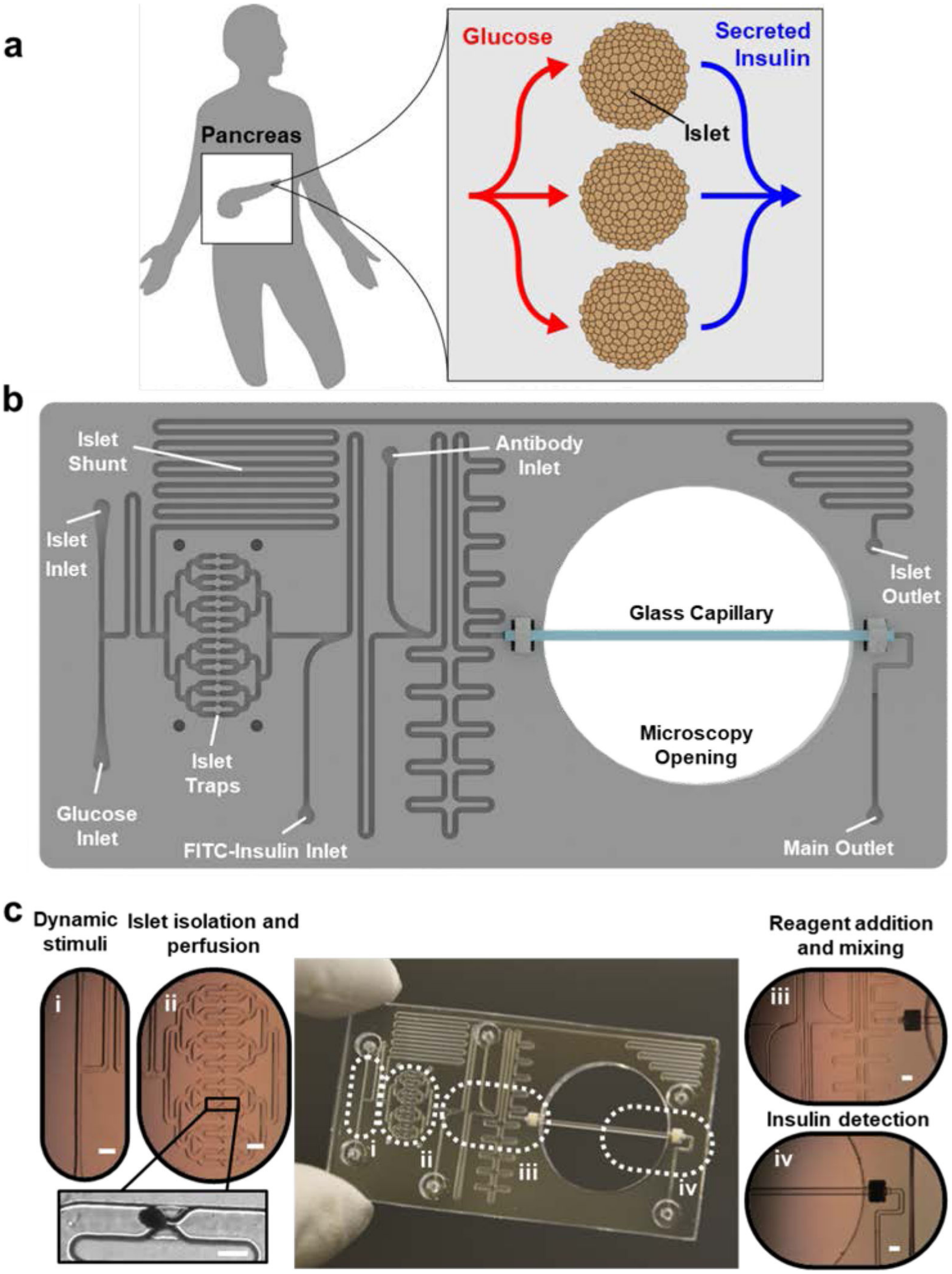

Figure 1 |. Islet on a Chip design.

a. Illustration of parallel glucose delivery (red lines) and insulin collection (blue lines) from native islets in a human pancreas. **b.** Overhead drawing of the “Islet on a Chip” with labeled perfusion channels and traps. **c.** Photograph of fabricated chip with optical micrographs of glucose inlets for islet stimulation (i), traps with a trapped human islet shown in the inset (ii), reagent inlets and mixing motifs (iii), and an integrated glass capillary for detection of optical signals for insulin sensing (iv). Main scale bars denote 1 mm, while scale bar for inset of ii indicates 400 μm.

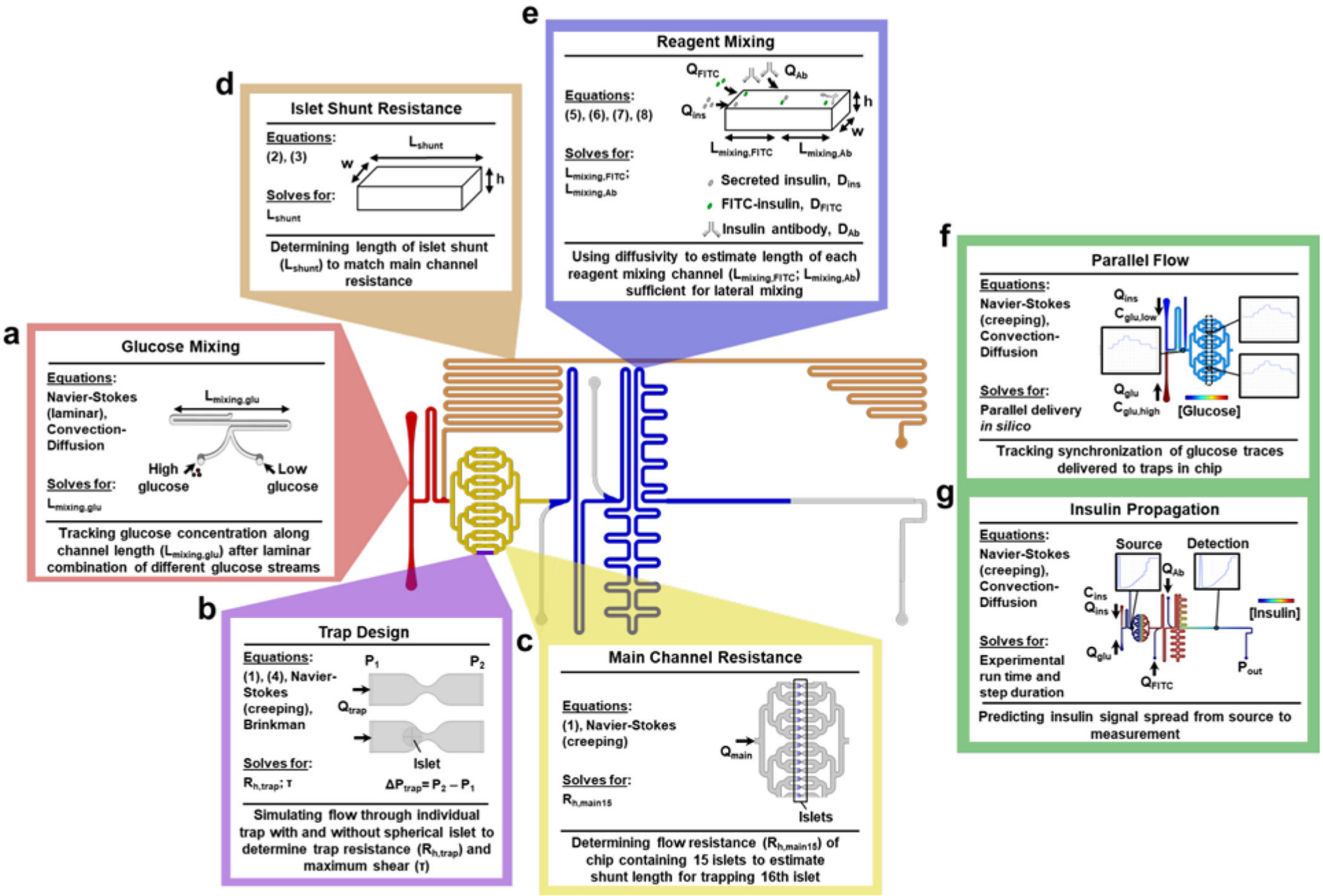

Figure 2 |. Modeling for chip feature design.

Graphical schematic outlining the model design for the ‘Islet on a Chip’ with specific regions highlighted. **a.** Glucose mixing channel. Three-dimensional flow and convection-diffusion modeled using CAD to ensure sufficient channel length ($L_{mixing,glu}$) for complete mixing of glucose input streams. **b.** Islet trap. Single traps were modeled with three-dimensional flow simulations to predict changes in pressure (ΔP), flow rate (Q_{trap}), resistance, and shear (τ) in the presence and absence of islets. Traps were designed to maximize inward flow, while retaining minimal shear. **c.** Main channels. Hydraulic resistance (R_{main}) through main chip channels was modeled with 15 occupied traps in two-dimensions using combined glucose and islet inlet flow (Q_{main}). **d.** Islet shunt. A rectangular channel with height (h) and width (w) was resistance-matched to R_{main} by setting its length (L_{shunt}) **e.** Reagent mixing channels. The lengths of the reagent mixing channels ($\mathrm{L}_{\mathrm{mixing\ ,FITC}}$ and $\mathrm{L}_{\mathrm{mixing\ ,Ab}}$) were determined using the molecular diffusivities of fluorescent reagents (D_{FITC} and D_{Ab}) and inlet flow rates (Q_{ins}, Q_{FITC}, and Q_{Ab}). **f.** Parallel flow. For total chip design, delivery of glucose pulses on the chip were simulated with a time-dependent, two-dimensional model of flow and convection-diffusion. Low ($c_{glu,low}$) and high ($c_{glu,high}$) concentrations of glucose were delivered at variable flow rates from the glucose and islet inlets (Q_{glu}, Q_{ins}). Graphic depicts the spatial concentration map of glucose at one time point of simulation of insulin and insets show traces of glucose concentrations at different locations on the chip. **g.** Insulin propagation. Model from panel f adapted to simulate insulin propagation in the chip based on a fixed concentration of insulin delivered from the islet inlet (c_{ins}). Flow from the regent inlets was also simulated (Q_{FITC}, Q_{Ab}), with outlet pressure (P_{out}) matched to atmospheric pressure. Graphic depicts the spatial concentration map of insulin at one time point of simulation of insulin and insets show concentration traces at the source and detection point.

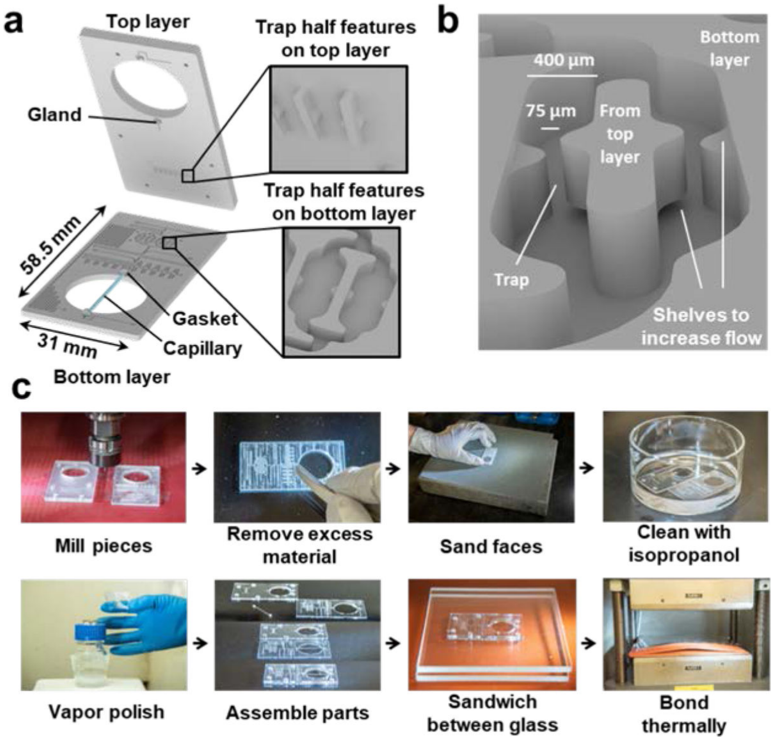

Figure 3 |. Scalable manufacturing of the Islet on a Chip.

a. Exploded view of the islet chip drawing in Figure 1b to show integration of the glass capillary and trap features on each layer before bonding. **b.** Angled, zoomed view of two adjacent islet traps in the islet chip drawing in Figure 1b to visualize channel and trap detail. Middle island between each pair of channels protrudes from the bottom surface of the top layer and fits into the channel to complete the trap during bonding. A small opening above or below each wall in the traps was designed to increase flow through the traps. **c.** Photographs of steps in chip fabrication. First, chip features are milled into polycarbonate and excess material is removed. Layers are then sanded, cleaned, and vapor polished. Finally, the capillary is assembled between polished layers and bonded together.

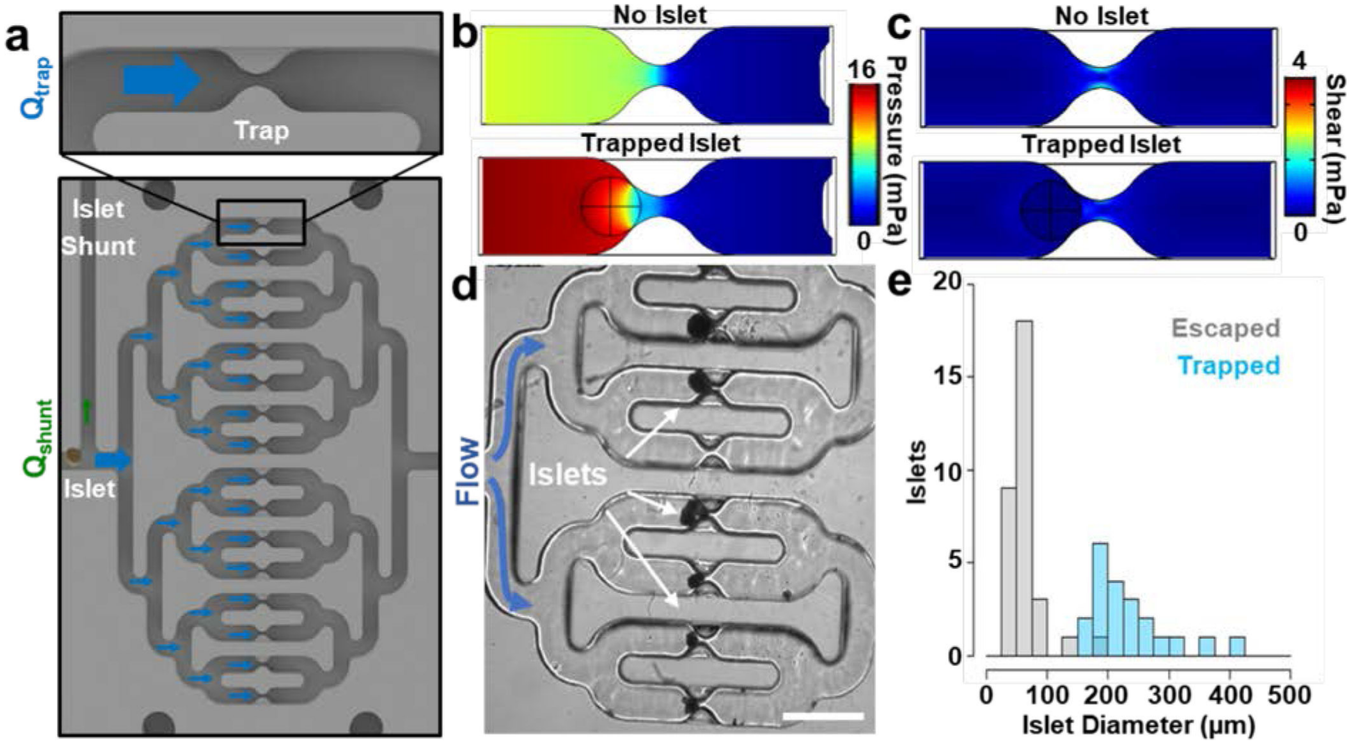

Figure 4 |. Hydrodynamic islet trapping in the Islet on a Chip.

a. Zoomed views of an islet trap (top) and the entire trap region (bottom) from the drawing of the chip in Figure 1b. Blue and green arrows indicate the direction and magnitude of flow through the trap regions (Q_{trap}) and islet shunt (Q_{shunt}), respectively. As islets settle into each trap, the portion of flow leading to the shunt increases. **b.** Horizontal cross section of a 3D model of pressure around a single trap either with (bottom) or without (top) a trapped islet. **c.** Horizontal cross section of a 3D model of shear around a single trap either with (bottom) or without (top) a trapped islet. In both c and d, the position of the trapped islet is indicated by the black circle and crosshair. **d.** A phase contrast micrograph of trapped human islets on the chip. Scale bar denotes 1 mm. **e.** A histogram showing the number of islets (n = 53 islets from 3 separate experiments) of different sizes that either escaped (gray bins) or were trapped (blue, semitransparent bins) after entering an unoccupied trap. Bin size is 25 μm.

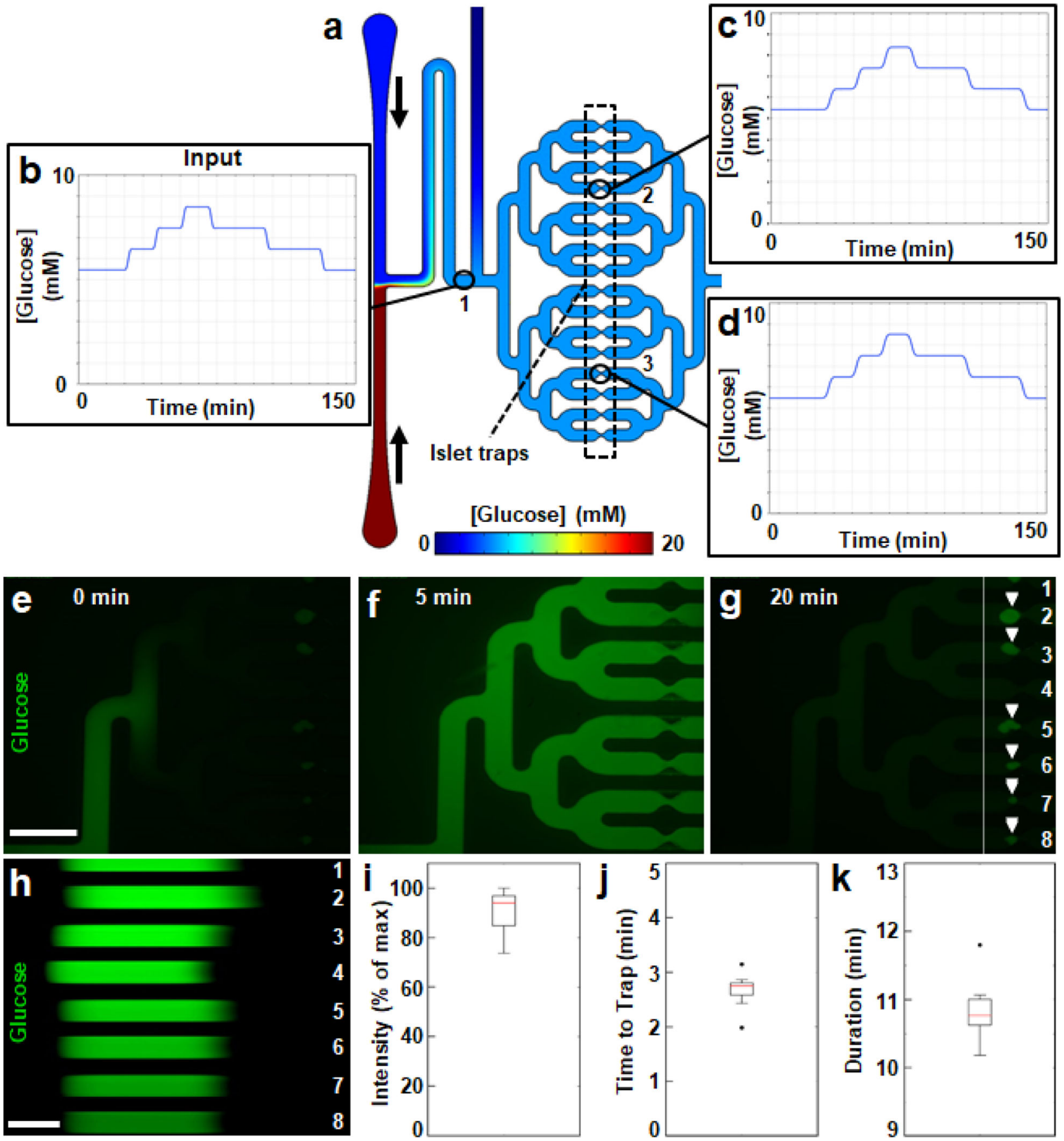

Figure 5 |. Parallel glucose delivery to isolated human islets in the chip.

a. Two-dimensional, time-dependent simulation of glucose diffusion through the trap region of the chip at an equilibrated glucose concentration of 5 mM. Simulated low (2.8 mM) and high (20 mM) glucose solutions entered the chip from the top and bottom inlets, respectively, with vertical black arrows to the right inlets indicating the direction of flow. The traps are indicated by a box with a dashed black outline and numbered black circles mark three points of interest in panels b-d. **b-d.** Plots of glucose pulses that were delivered to the chip in the simulation. Data points in each plot reflect the concentrations of glucose in the chip at points either immediately past the glucose mixing region (b, point “ 1”), or at traps in the top (c, point “2”) or bottom (d, point “3”) branches. **e-g.** Fluorescent micrographs from Movie S1 of the start (e, time = 0 minutes), middle (f, time = 5 minutes), and end (g, time = 20 minutes) of a ten-minute pulse of fluorescent glucose (green) traversing the trap region of the chip. Scale bar denotes 1 mm. White arrowheads in panel g indicate the positions of trapped islets. The eight parallel channels shown are numbered in white and a vertical white line indicates a cross section of interest in panel h. **h.** Time-lapse (kymograph) of Movie S1 at the cross section of the imaged area indicated by the white vertical line in panel g. Scale bar denotes 3 minutes and time is portrayed from left to right. **i-k.** Boxplots of maximum intensity (i), onset (j), and duration (k) of fluorescent glucose pulses across the eight channels in panel h.

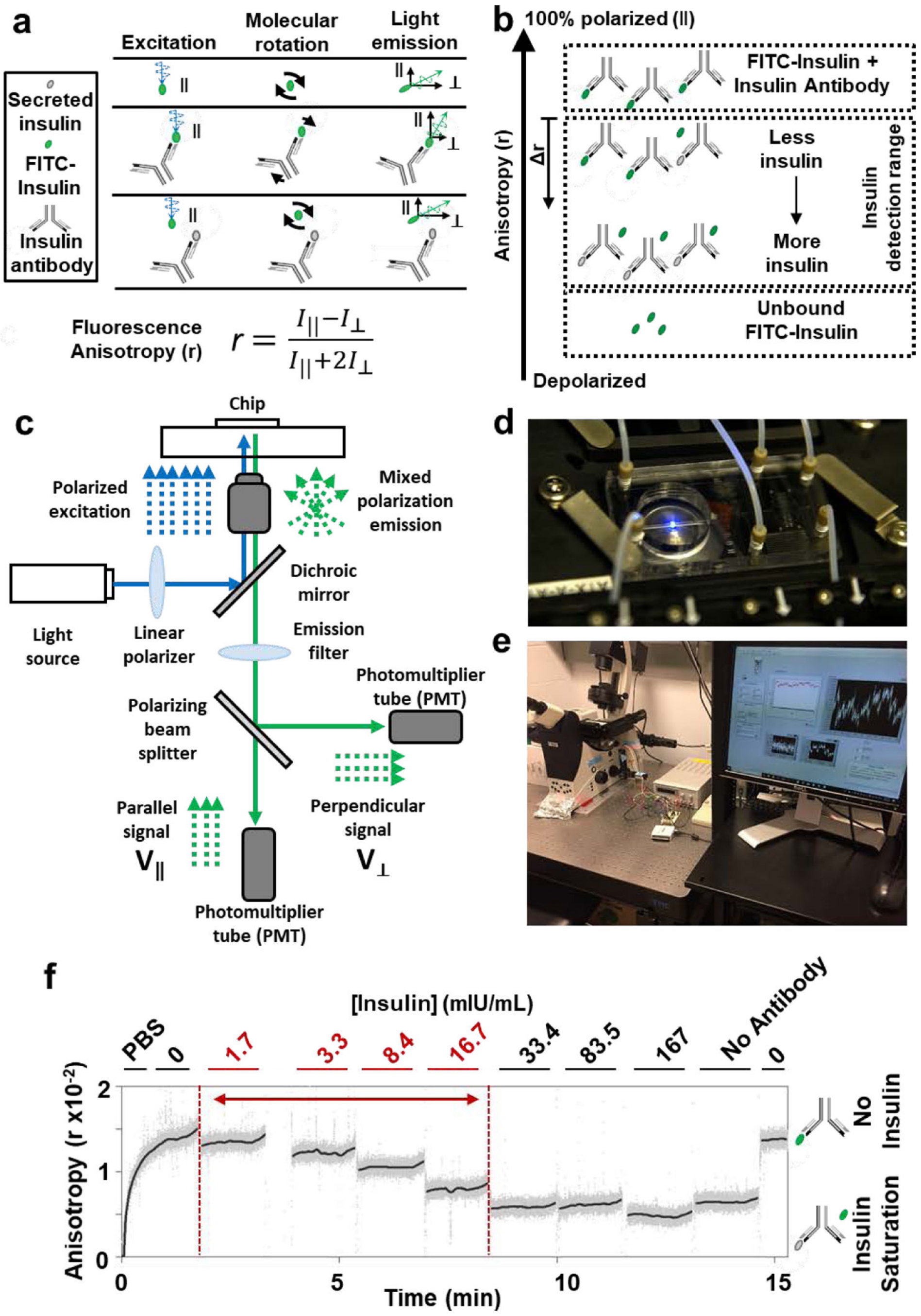

Figure 6 |. Sensing insulin by fluorescence anisotropy.

a. Illustration of the physical principle of fluorescence anisotropy for insulin detection. FITC-insulin (green oval) and insulin antibody (gray Y) are added to secreted insulin (gray oval). Molecular behavior of FITC-insulin (top), a mixture of antibody and FITC-insulin (middle), and a mixture of all three molecules (bottom). Polarized light (blue wave) excites FITC-insulin molecules that rotate in solution (black arrows). Vertical and horizontal black arrows show the parallel **(∥)** and perpendicular (⊥) components, respectively, of fluorescent emissions (green waves). Perrin equation (far bottom) for fluorescence anisotropy (*r*) is a ratio of fluorescent light intensity parallel to the exciting light ($I_{\perp}$) to the total light intensity. **b.** Illustration showing relative anisotropy (*r*) values for the insulin detection assay. Lower anisotropies indicate higher concentrations of secreted insulin. An anisotropy shift (Δr, downward arrow) can be calculated from the case where no insulin is present in the system. **c.** Diagram of the optical sensor used to measure fluorescence anisotropy on the chip. **d.** Photograph of the chip with flow connections and positioned in the optical sensor. **e.** Photograph of the recording setup. **f.** A calibration of the optical sensor with insulin standards as well as solutions without insulin (“0”) or without insulin antibody (“No Antibody”). Solutions were mixed offline and flowed through a glass capillary positioned in the sensor. 1 nM Insulin = 167 μIU.

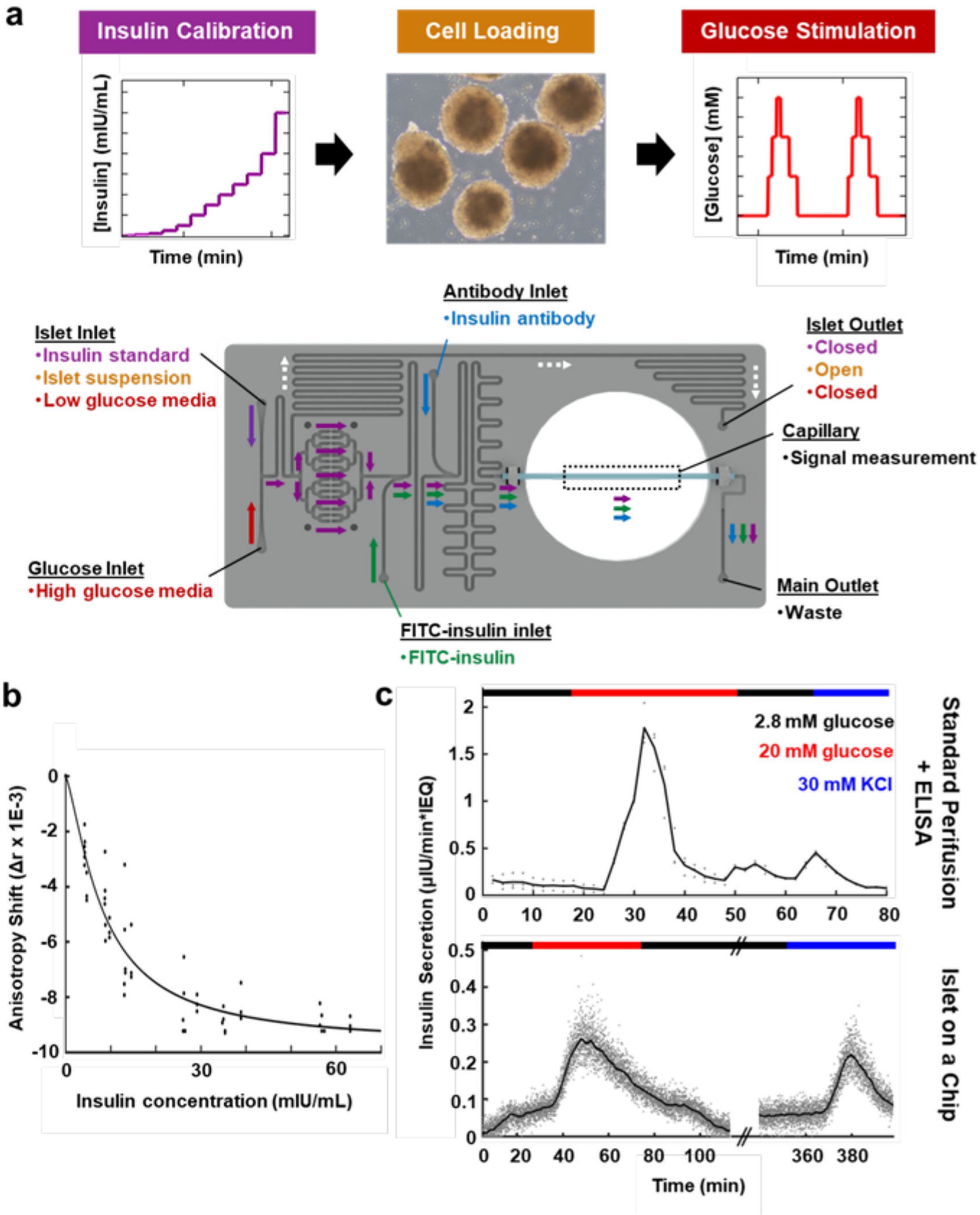

Figure 7 |. Measuring glucose stimulated insulin secretion from primary human islets.

a. Diagram of experimental protocol and chip setup highlighting the three main stages of chip operation – insulin calibration (purple), cell loading (orange), and glucose stimulation (red). During insulin calibration, a fixed amount of insulin was introduced into the chip from the islet inlet and combined with medium lacking insulin from the glucose inlet at different flow rate ratios to produce controlled concentrations of insulin on the chip. The fluorescent anisotropy for each concentration of insulin was determined by fluorescence measurements in the capillary. During cell loading, islets suspended in medium without insulin were introduced into a reservoir connected to the islet inlet and allowed to flow through the chip towards the islet traps. The islet outlet was also opened to allow an escape for islets in excess of those captured by the traps. After traps had been filled with islets, the islet outlet was again closed. Dynamic glucose stimulation of the islets was achieved by mixing low glucose medium introduced through the islet inlet with high glucose medium from the glucose inlet at different flow ratios. FITC-insulin (green) and insulin antibody (blue) were continuously introduced and mixed with insulin during both the insulin calibration and the glucose stimulation. **b.** Aggregated insulin calibration data used for quantifying islet insulin secretions (n = 9 calibrations from 4 separate sensor calibration experiments). **c.** Measured secretion rate of insulin from the same batch of primary human islets loaded into a standard perifusion system (top) or onto the Islet on a Chip (bottom) at low (2.8 mM, black) and high (20 mM, red) concentrations of glucose. 30 mM KCl treatment (blue) was also delivered as a positive control for insulin secretion. Gray dots indicate raw measurements from samples collected every 2 minutes for the perifusion system or from continuous flow at 1 Hz for the Islet on a Chip. Black line depicts either the average of three replicates (top) or a moving point average across a 2-minute window (bottom). Parallel lines indicate a break in the horizontal axis (bottom) for protocol alignment of the two methods. 1 nM Insulin = 167 μIU.

Table 1 |

Design Criteria for Islet on a Chip

Design Criteria	Approach
Autoclavable	• Polycarbonate
Optically transparent material	
Automated islet loading	• Hydrodynamic trapping
Sufficient oxygen (3.6 pmol/min*islet) [35]	• Oxygenated medium at 1.4 μL/min (24.3 pmol/min*trap) [36]
Homogeneous glucose delivery	• Flow resistance-matched channels leading to isolated islets
Dynamic glucose delivery	• Two inlets for mixing high and low glucose solutions
Continuous on-chip insulin sensing	• On-chip competitive binding and detection of fluorescence anisotropy
Detectable insulin output	• Low flow rate (1.6 μL/min)
Short lag in glucose delivery and insulin detection	• Minimal internal volume

Table 2 |

Islet on a Chip Device Comparison

Reference	Material	Insulin Quantification	Islet Loading	Parallel Perifusion	Islet Source
This work	Thermoplastic	On-chip	Automated	Yes	Human
61	Thermoplastic	Offline kit	Manual	No	Human/Mouse
13,19,25	Glass	On-chip	Manual	Yes	Mouse
14–18,20–22	Glass	On-chip	Manual	No	Human/Mouse
23	PDMS	On-chip	Manual	No	Mouse
10,28,48	PDMS	Offline kit	Manual	No	Rat/Mouse
8,11,12,26,27,44,47,49	PDMS	Offline kit	Automated	No	Human/Mouse

Table 3 |

Insulin Quantification by ELISA versus the Islet on a Chip

Feature	ELISA	Islet on a Chip
Measurement Frequency	Discrete	Continuous
Minimum Sample Volume	25 μL	10 nL
Dynamic Range[**]	4–500 nIU [***]	10–300 nIU

[*] 1 Hz sampling rate

[**] Normalized by minimum sample volume

[***] 1 nM Insulin = 167 μIU.